

Predicting Crystal Structures and Ionic Conductivities in $\text{Li}_3\text{YCl}_{6-x}\text{Br}_x$ Halide Solid Electrolytes Using a Fine-Tuned Machine Learning Interatomic Potential

Jonas Böhm^{*,†} and Aurélie Champagne^{*,†}

[†]*Université de Bordeaux, CNRS, Bordeaux INP, ICMCB, F-33600 Pessac, France*

[‡]*Réseau sur le Stockage Electrochimique de l'Energie (RS2E), CNRS FR 3459, Cedex 1, F-80039 Amiens, France*

E-mail: jonas.bohm@icmcb.cnrs.fr; aurelie.champagne@icmcb.cnrs.fr

Abstract

Understanding ionic transport in halide solid electrolytes is essential for advancing next-generation solid-state batteries. This work demonstrates the effectiveness of fine-tuning the Crystal Hamiltonian Graph Network (CHGNet) universal machine learning interatomic potential to accurately predict total energies, relaxed geometries, and lithium-ion dynamics in the ternary halide family $\text{Li}_3\text{YCl}_{6-x}\text{Br}_x$. Starting from experimentally refined disordered structures of Li_3YCl_6 and Li_3YBr_6 , we present a strategy for generating ordered structural models through systematic enumeration and energy ranking, providing realistic structural models. These serve as initial configurations for an iterative fine-tuning workflow that integrates molecular dynamics simulations and static density functional theory calculations to achieve near-ab initio accuracy at four orders of magnitude lower computational cost. We further reveal the influence

of composition (varied x) on the predicted phase stability and ionic conductivity in $\text{Li}_3\text{YCl}_{6-x}\text{Br}_x$, demonstrating the robustness of our approach for modeling transport properties in complex solid electrolytes.

Introduction

Lithium-ion (Li-ion) batteries play a crucial role in modern energy storage, powering consumer electronics, electric vehicles, and grid-level applications thanks to their high gravimetric energy density and long life cycle. They not only enable the transition toward sustainable mobility but also help stabilize power grids by compensating for the intermittency of renewable energy sources.^{1,2} A conventional Li-ion battery consists of a negative electrode, liquid electrolyte, separator, and positive electrode. In contrast, all solid state batteries (ASSBs), replace the flammable liquid electrolyte and polymer separator with a solid electrolyte (SE), offering enhanced safety, higher energy and power density, faster charging,³ and reduced cross-contamination between electrodes.⁴ However, realizing these advantages introduces major materials and engineering challenges,⁴ including: (1) developing solid composite cathodes that operate reliably under minimal pressure (< 0.1 MPa); (2) identifying SEs with high ionic conductivity, broad electrochemical stability window, mechanical robustness, and low cost; (3) ensuring stable, low-resistance interfaces between SEs and electrodes; and (4) implementing high-capacity anodes such as Li metal or Si-based materials for enhanced battery energy density. Among these, the SE is central, as it governs ion transport, interfacial stability, and mechanical integrity – directly impacting the first three challenges.⁴⁻⁶ An ideal SE should combine high ionic conductivity (≥ 10 mS cm^{-1}), negligible electronic conductivity, mechanical strength sufficient to suppress dendrite growth, and (electro)chemical stability across the 0 – 5 V vs. Li/Li⁺ window.⁴

Recently, ternary metal halides with general formula $\text{Li}_3\text{MA}_{6-x}\text{B}_x$ (M = Y, Er, and In; A, B = Cl, Br, I) have emerged as highly promising SEs.⁷ These materials offer a unique

combination of electrochemical stability compatible with 4 V-class cathodes, mechanical and thermal robustness, and room temperature Li^+ conductivities exceeding 1 mS cm^{-1} .⁷ Their ionic conductivity can be further tuned through compositional substitution and synthesis control,^{7–10} providing a versatile compositional design space for performance optimization. For instance, van der Maas *et al.* observed in the $\text{Li}_3\text{YCl}_{6-x}\text{Br}_x$ (LYCB) series that ionic conductivity peaks at 5.36 mS cm^{-1} near $x = 4.5$.⁹ They also observed a structural transition from trigonal ($P\bar{3}m1$) to monoclinic ($C2/m$) symmetry within $1.5 < x < 3$; however the interplay between this structural change and the enhancement in ion transport remains unclear.

Designing halide electrolytes with increased ionic conductivity thus requires a microscopic understanding of how composition, structure, and anion substitution modulate Li^+ migration pathways. Yet, the vast compositional space and experimental limitations in directly probing atomic-scale diffusion processes necessitate integrated computational-experimental approaches. Atomistic modeling, especially molecular dynamics (MD), provides valuable insights into Li^+ diffusion mechanisms and structure-transport relationships, enabling to narrow down the most promising compositions.

The accuracy of MD simulations relies on the description of the underlying potential energy surface (PES), traditionally obtained either from first-principles methods such as density functional theory (DFT) or from empirical force fields. While DFT offers high accuracy, it is computationally prohibitive for the long timescales required to capture diffusion processes (on the order of several nanoseconds). Machine learning interatomic potentials (MLIPs) have recently emerged as a powerful alternative, combining near-DFT accuracy with several orders of magnitude lower computational cost.¹¹ MLIPs approximate the PES by mapping atomic coordinates $[\mathbf{r}_v]$ and atomic numbers $[Z_v]$ to total energies E ,¹² using local environment descriptors and machine learning (ML) regression schemes. Their linear scaling with system size and parallelizability make them ideally suited for large-scale MD simulations.¹³ The performance of an MLIP critically depends on its training data; and large datasets are

often required to achieve robust generalization. Pretrained universal machine learning interatomic potentials (uMLIPs) – such as Materials 3-body Graph Network (M3GNet),¹⁴ Crystal Hamiltonian Graph Network (CHGNet),¹⁵ and Scalable EquiVariance-Enabled Neural Network (SevenNet)¹³ – are trained on extensive materials databases encompassing diverse chemical systems,^{16–18} and can, in principle, generalize across chemistries. However, their transferability to new material classes such as halide SEs remains uncertain. Thus, system-specific fine-tuning is often required to achieve reliable quantitative predictions.^{19–22}

In this work, we investigate lithium-ion transport in halide SEs by elucidating how crystal structure, stoichiometry, and anion substitution govern ionic conductivity within the LYCB family. We first present an efficient and accurate enumeration-ranking procedure to systematically explore all possible ordered configurations starting from disordered experimentally-refined structures. We then develop an iterative fine-tuning procedure, inspired by active-learning loops,^{23–26} that integrates targeted DFT data generation with adaptive model refinement. Using this approach, we fine-tune the pretrained CHGNet model¹⁵ to reproduce the PES of LYCB compounds with high-fidelity, enabling nanosecond MD simulations at a computational cost roughly 10^4 times lower than DFT. Finally, we benchmark the fine-tuned CHGNet model against its pretrained counterpart and the state-of-the-art SevenNet potential¹³ (pretrained on an even larger dataset including out-of-equilibrium structures¹⁸). Our results provide fundamental insights into Li^+ transport and phase stability across halide compositions, and establishes a general, data-efficient strategy for adapting uMLIP to new material systems – a strategy significantly more effective than training a ML model from scratch. Overall, this framework paves the way for accelerated discovery and rational design of next-generation SEs for ASSBs.

Results and Discussion

Structure enumeration and energy-based ranking

A key initial challenge in modeling halide SEs lies in defining suitable starting structures. Experimentally refined models of Li_3YCl_6 (LYC) ($P\bar{3}m1$) and Li_3YBr_6 (LYB) ($C2/m$) exhibit partial occupancies on Li and Y sites, reflecting intrinsic disorder (Figure 1). Determining the lowest-energy ordered configuration among all possible arrangements requires evaluating the total energy of a vast amount of configurations quickly approaching infinity with increasing supercell size. Conventional Ewald-based electrostatic ranking^{27,28} offers a rapid but approximate criterion that neglects many-body interactions, whereas DFT provides higher accuracy but is computationally prohibitive for such vast configurational spaces. This configurational complexity is not unique to halide conductors and also arises in disordered oxide and sulfide electrodes and electrolytes. Consequently, many of these compounds are absent from large materials databases such as the Materials Project,¹⁶ since their accurate representation demands large supercells and explicit sampling of disorder.

To overcome these limitations, we employ a uMLIP – namely M3GNet model¹⁴ – to efficiently screen and rank candidate configurations. Starting from $1 \times 1 \times 2$ supercells of the experimental LYC and LYB models,⁸ all symmetrically distinct orderings are generated using the *enumlib* library²⁹ (Figure 1). A total of $\sim 60,000$ LYC and $\sim 200,000$ LYB structures are optimized using M3GNet and ranked according to their predicted total energy. From these, we identify the 20 lowest-energy structures and perform subsequent DFT optimization to validate their energetic ordering. This procedure yields low-energy ordered structures for both LYC and LYB, denoted LYC0 ($P\bar{3}c1$) and LYB0 ($C2$), respectively – and more importantly provides a physical starting point for our subsequent MD simulations.

We extend this approach to mixed-halide compositions, LYCB, by systematically substituting Cl/Br in both parent lattices, followed by enumeration and M3GNet-based optimiza-

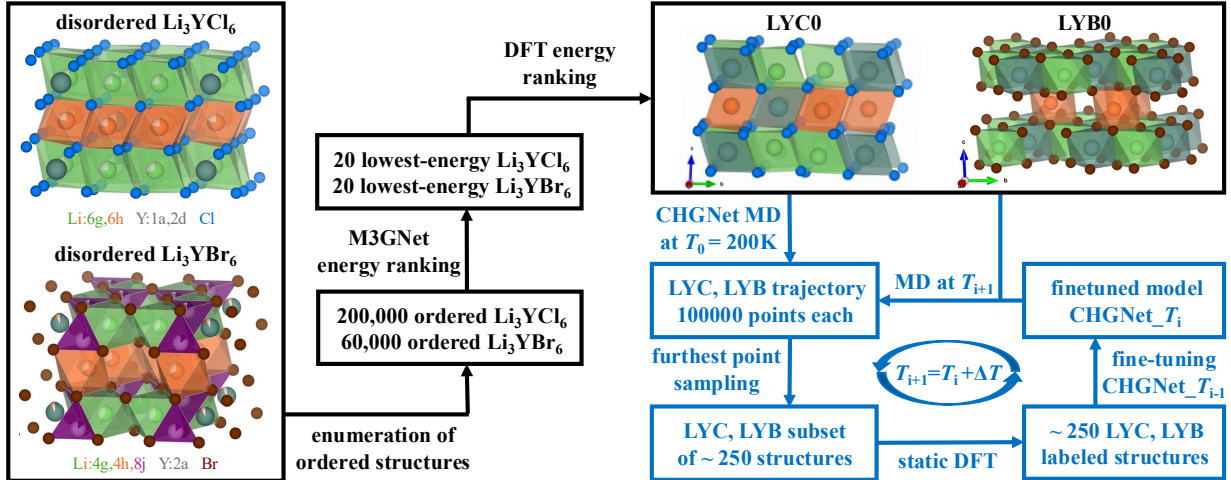


Figure 1: Global workflow combining the enumeration-ranking strategy (black boxes) with the uMLIP fine-tuning framework (blue boxes). Starting from experimentally resolved structures⁸ – which exhibit partial occupancies – symmetry-distinct ordered configurations are enumerated and ranked using the M3GNet uMLIP. Additional DFT calculations are performed on the lowest-energy configurations to identify the ground-state ordered configuration – subsequently used as a starting configuration in the fine-tuning procedure. The fine-tuning procedure involves a series of CHGNet-driven MD simulations (with LAMMPS) at finite temperatures (T_i). For each MD run (1,000,000 steps), DFT calculations (with VASP) are performed on a subset of structures to obtain additional training data that are used to fine-tune CHGNet model. Computational details are provided in the Computational Methods.

tion and energy ranking. Across the full composition range ($x = 0$ to 6, step 0.5), we obtain 13 ordered derivatives for each parent phase. These ordered models provide consistent, low-energy starting points, which are subsequently used in the uMLIPs fine-tuning procedure and for lithium-ion diffusion simulations.

CHGNet performance for energy and volume prediction

To assess baseline performance, we benchmark the pretrained uMLIP CHGNet against DFT reference data.

For 0 K-structures, static CHGNet calculations reproduce energetic trends of LYCB compounds with mean absolute errors (MAEs) below 11 meV atom⁻¹ (Figure S1). Furthermore, CHGNet structure optimizations predict volumes and cell parameters within 5% of the DFT

values (Figure S7), while being over 2,000 times faster to compute (≈ 50 s CPU vs. ≈ 33 h CPU per structure using DFT). CHGNet’s accuracy for energy and structure predictions at finite temperature is benchmarked in Figure 2. In Figure 2(a), we compare total energies predicted by CHGNet (circles) with DFT references (black crosses) for 880 LYC and 880 LYB structures extracted from finite-temperature MD simulations. While CHGNet performs remarkably well at low temperature, energy predictions start to deviate at $T \geq 600$ K, with errors in the energy predictions as large as 70 meV atom^{-1} .

To assess CHGNet’s accuracy in volume prediction, we perform MD simulations in the NpT ensemble and obtain equilibrated structures for LYC and LYB at targeted temperatures up to 650 K. Figures 2(d) and (e) compare CHGNet predicted volumes with SevenNet data and available experimental values: exp (neutron diffraction),⁸ exp_2 (neutron diffraction), exp_2* (synchrotron X-ray diffraction on higher crystalline sample),¹⁰ and exp_3 (X-ray diffraction).⁷ While CHGNet matches SevenNet volumes within 2 – 8% at low temperature, it significantly overestimates volumes at higher temperature. Moreover, above 500 K, some simulations became unstable, with diverging volume fluctuations (indicated by a star in Figure 2(e)). These failures highlight CHGNet’s limitations in capturing thermodynamic and structural diversity encountered at finite temperature, underscoring the need for system-specific fine-tuning.

Fine-tuning CHGNet with finite-temperature data

To address this, we implement an iterative fine-tuning protocol that augments the training dataset with targeted DFT data for LYC and LYB compounds (see Figure 1 and Computational Methods). Four progressively refined models – CHGNet_200K, _400K, _600K, and _800K – are trained by successively incorporating structures from MD trajectories at increasing temperature (Figure 2(a)), starting from the fine-tuned model from the previous iteration. In the SI, we discuss the effect of fine-tuning CHGNet with all accumulated training data at once. The present active-learning-inspired refinement expands the configu-

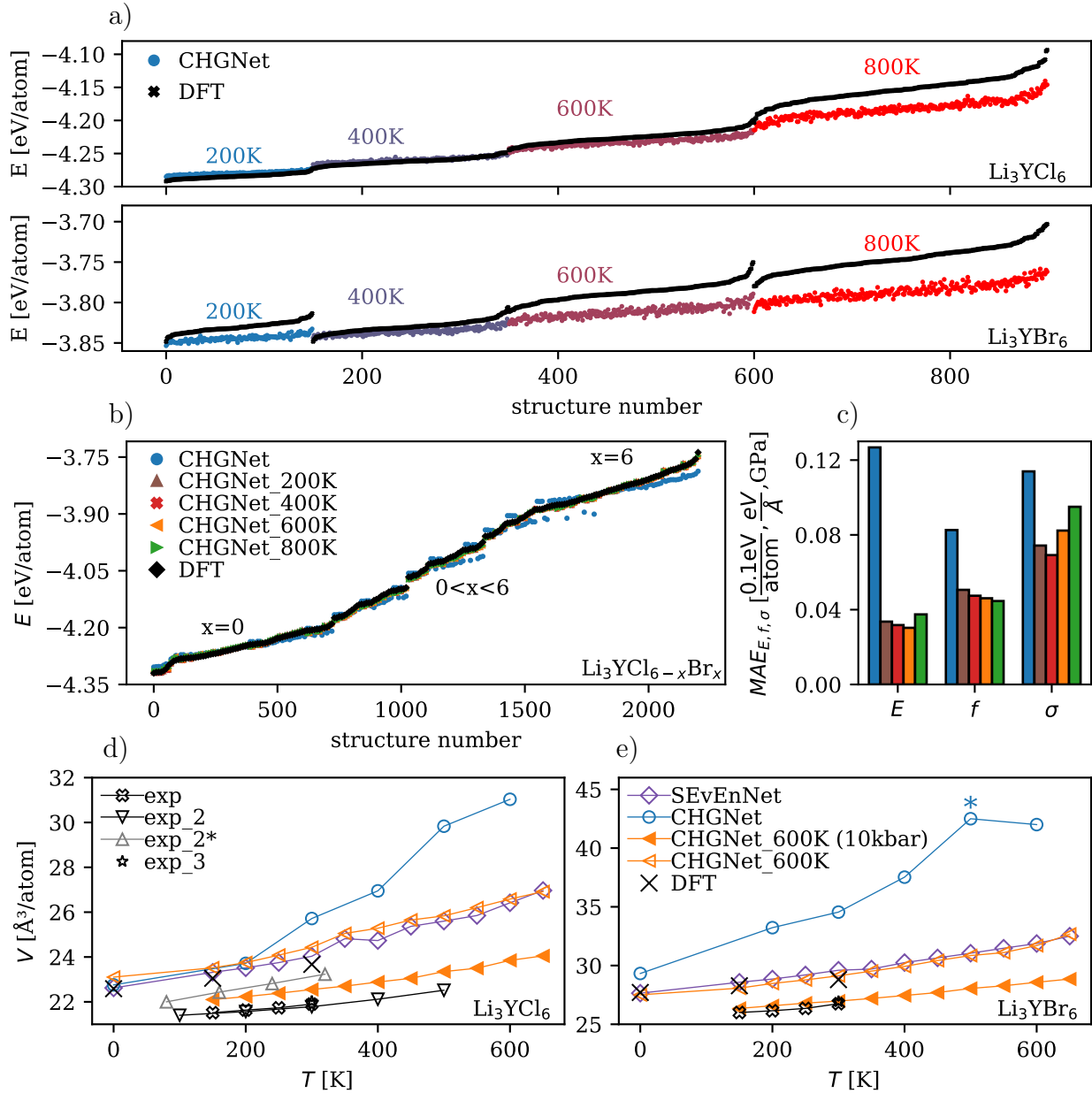


Figure 2: (a) Total energies predicted with CHGNet (colored circles), compared to DFT reference data (black crosses), for a series of finite-temperature structures generated during the fine-tuning procedure in Figure 1. (b) Benchmark of the pretrained and fine-tuned CHGNet potentials for total energy prediction of LYC, LYB, and LYCB, compared to DFT data. (c) MAEs on energy (in 0.1 eV/atom), forces (in eV/ \AA), and stress (in GPa) for the various models with the same color-code as in (b). (d) and (e) Average volume/atom resulting from the NpT equilibration MD runs, using the pretrained CHGNet (blue circles) and fine-tuned CHGNet_600K potentials (orange triangles, solid for high pressure of 10kbar), compared to SevenNet predictions (purple diamonds), DFT calculations (black crosses), and experimental data (black and gray markers) from Refs. 7,8,10. Note the blue star in (e) indicates an unstable simulation with nonphysical cell volume, which is scaled here by 0.1.

rational diversity of the training data and significantly improves agreement with DFT across all metrics, as shown for an independent test-dataset of LYCB structures from 0 K to 800 K in Figures 2(b) and (c). Remarkably, although CHGNet is fine-tuned only on the LYC and LYB endpoints, it retains high predictive accuracy for finite-temperature intermediate compositions. Among all models, CHGNet_600K offers a good balance between the metrics, with energy, force, and stress MAEs below $3.5 \text{ meV atom}^{-1}$, 50 meV \AA^{-1} , and 85 MPa , respectively – comparable to state-of-the-art MLIPs.³⁰ Importantly, CHGNet_600K remains stable during long NpT MD runs up to 800 K, where the pretrained model failed. Subsequent analyses are therefore performed using CHGNet_600K, if not otherwise stated.

Fine-tuning improves not only static energies but also thermodynamic observables. Figures 2(d), (e) and Tables 1, 2 compare the average volumes predicted by CHGNet, CHGNet_600K, and SevenNet for LYC and LYB. While the pretrained model systematically overestimates the reference volumes from SevenNet and DFT by 2-8% at 0 K and up to 25-40% at higher temperature, the fine-tuned CHGNet_600K model brings the predictions into near-quantitative agreement with both SevenNet and direct *ab initio* calculations (see Computational Methods), with deviations within 2%. This level of consistency between CHGNet_600K and DFT indicates that the fine-tuned model has reached the accuracy ceiling expected for a MLIP trained on first-principles data. Relative to experiment, CHGNet_600K reproduces equilibrium volumes and thermal expansion trends (*i.e.*, the slope in Figures 2(d), (e)) within $\leq 10\%$ – within $\leq 5\%$ for highly crystalline samples¹⁰ –, which is comparable to typical DFT-level agreement.

The remaining 5 – 10% volume overestimation relative to experiment is expected and can be attributed to two main factors. First, simulated structures correspond to ideal, fully crystalline cells, whereas experimental samples often exhibit lower crystallinity, defects, or microstrain that reduce the measured average volume. Second, the underlying PBE(+U) functional used to generate the training data is known to systematically overestimate equi-

Table 1: For the LYC system: Predicted volumes (V , in $\text{\AA}^3/\text{atom}$) at $T = 0, 200, 300, 400,$ and 600 K , activation energies (E_A , in eV), and room-temperature Li conductivities ($\sigma_{300\text{K}}$, in mS cm^{-1}), obtained with CHGNet, CHGNet_600K, and SevenNet, and compared to AIMD³¹ and experimental data from Refs. 7–10. We note that these values were partly extracted from figures, when not stated directly in the references.

Models	p [bar]	V [$\text{\AA}^3/\text{atom}$]					E_A [eV]	$\sigma_{300\text{K}}$ ($\sigma_{\min}; \sigma_{\max}$) [mS cm^{-1}]
		0 K	200 K	300 K	400 K	600 K		
CHGNet	1	22.8	23.7	25.7	26.9	31.0	-	-
SevenNet	1	22.6	23.5	24.0	24.7	26.4	0.17 ± 0.01	122 (107; 183)
CHGNet_600K	1	23.1	23.8	24.4	25.3	26.6	0.12 ± 0.01	331 (295; 485)
CHGNet_600K	10^4	-	22.2	22.6	22.9	23.9	0.24 ± 0.01	15.7 (13.6; 23.5)
AIMD ³¹	-	22.4	-	-	-	-	0.19 ± 0.03	14.0 (4.5; 47)
exp ⁸	-	-	21.6	21.9	-	-	0.41	0.09
exp* ⁸	-	-	-	-	-	-	0.44	0.06
exp** ⁸	-	-	-	-	-	-	0.49	0.04
exp_2 ¹⁰	-	-	21.6	21.8	22.1	-	0.7	0.14
exp_3 ⁷	-	-	-	22.0	-	-	0.4	0.51
exp_3* ⁷	-	-	-	-	-	-	0.6	0.04
exp_4 ⁹	-	-	-	22.0	-	-	0.7	0.05

librium volumes.³² Consistent with this interpretation, applying a moderate external pressure of 10 kbar during MD simulations brings the predicted volumes into closer agreement with experiment. In subsequent transport analyses, we therefore consider Li-ion dynamics in the NVT ensemble starting from two equilibrated configurations: (1) cells relaxed at 1 bar – representing fully predictive simulations at the DFT-consistent volume – and (2) cells relaxed at 10 kbar – yielding volumes closer to experiment and thus more realistic ionic conductivities.

Lithium-ion diffusion in LYC and LYB compounds

Using CHGNet_600K, we perform 2 ns-long NVT MD simulations in NpT -equilibrated cells at temperatures ranging from 400 to 750 K. From these simulations, we quantify Li-ion transport in LYC and LYB by extracting self-diffusion coefficients (D), activation energies

Table 2: For the LYB system: Predicted volumes (V , in $\text{\AA}^3/\text{atom}$) at $T = 0, 200, 300, 400,$ and 600 K, activation energies (E_A , in eV), and room-temperature Li conductivities ($\sigma_{300\text{K}}$, in mS cm^{-1}), obtained with CHGNet, CHGNet_600K, and SevenNet, and compared to AIMD³¹ and experimental data from Refs. 7–9. We note that these values were partly extracted from figures, when not stated directly in the references.

Models	p [bar]	V [$\text{\AA}^3/\text{atom}$]					E_A [eV]	$\sigma_{300\text{K}}$ ($\sigma_{\min}; \sigma_{\max}$) [mS cm^{-1}]
		0 K	200 K	300 K	400 K	600 K		
CHGNet	1	29.3	33.2	34.5	37.5	42.0	-	-
SevenNet	1	27.6	28.9	29.6	30.2	31.9	0.20 ± 0.01	42.1 (33.1; 79.6)
CHGNet_600K	1	27.5	28.5	29.1	29.9	31.7	0.25 ± 0.01	19.5 (15.4; 35.1)
CHGNet_600K	10^4	-	26.6	27.0	27.4	28.6	0.36 ± 0.02	0.58 (0.37; 1.66)
AIMD ³¹	-	26.9	-	-	-	-	0.28 ± 0.02	2.20 (0.70; 7.3)
exp ⁸	-	-	26.1	26.8	-	-	0.36	0.3
exp* ⁸	-	-	-	-	-	-	0.34	1.4
exp** ⁸	-	-	-	-	-	-	0.21	4.3
exp_3 ⁷	-	-	-	26.9	-	-	0.37	0.72
exp_3* ⁷	-	-	-	-	-	-	0.31	1.7
exp_4 ⁹	-	-	-	-	-	-	0.33	4.7

(E_A), and room-temperature ionic conductivities ($\sigma_{300\text{K}}$) (Figures 3, 4, and Tables 1, 2).

For 1 bar-equilibrated cells, we obtain $E_A = 0.12 \pm 0.01$ eV (0.25 ± 0.01 eV) and $\sigma_{300\text{K}} \sim 331 \text{ mS.cm}^{-1}$ ($\sim 20 \text{ mS.cm}^{-1}$) for LYC (LYB), indicated by empty orange triangles in Figure 3. These values are comparable in magnitude to the SevenNet predictions and about one order of magnitude higher than the ab-initio molecular dynamics (AIMD) results reported in Ref. 31, which were obtained from NVT simulations using 0 K DFT optimized cells (without NpT cell equilibration) – effectively imposing a large internal pressure. When using cells compressed to near-experimental volumes ($p=10$ kbar, filled orange triangles), Li-ion mobility decreases, yielding $E_A = 0.24 \pm 0.01$ eV (0.36 ± 0.02 eV) and $\sigma_{300\text{K}} \sim 15.7 \text{ mS.cm}^{-1}$ ($\sim 0.6 \text{ mS.cm}^{-1}$) for LYC (LYB), in much better agreement with the AIMD data. Simulated conductivities for LYC exceed experimental values obtained via electrochemical impedance spectroscopy near 300 K,^{7–10} reflecting an overestimation when extrapolating higher-temperature diffusivities to room temperature. This discrepancy is consistent with the two diffusion

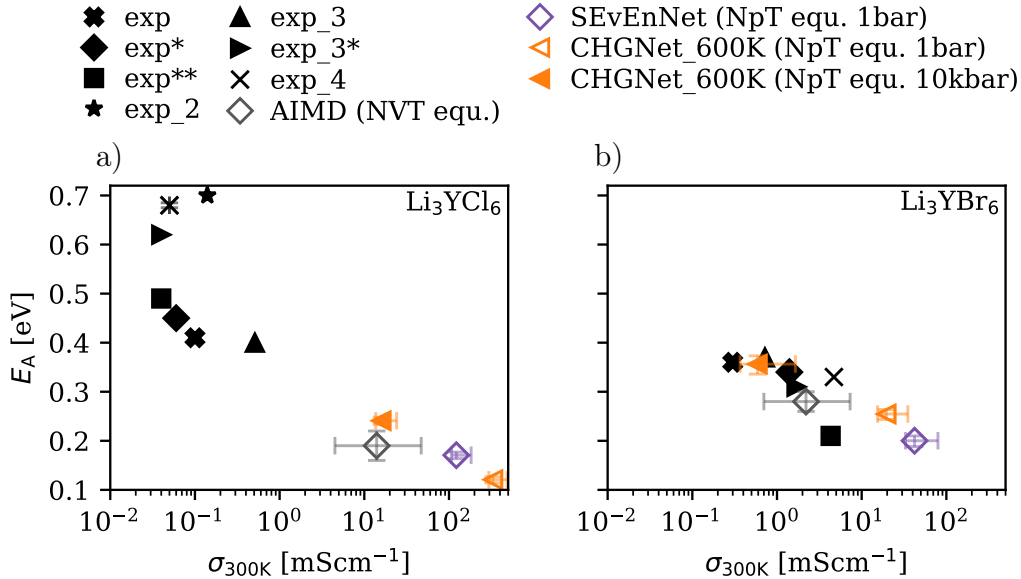


Figure 3: For (a) LYC and (b) LYB, we report the activation energy (E_A) and room-temperature ionic conductivity (σ_{300K}), obtained from MD simulations in the NVT ensemble, using CHGNet, CHGNet_600 K, and SevenNet. The simulations are conducted in NpT -equilibrated cells under $p=1$ bar (empty symbols) and $p=10$ kbar (filled orange triangles). Error bars originate from the variances in the diffusion coefficients that are estimated according to Ref. 33. We compare our predictions to AIMD³¹ and experimental values: exp, exp*, exp** (*different synthesis);⁸ exp_2;¹⁰ exp_3, exp_3* (*different synthesis);⁷ exp_4.⁹

regimes observed experimentally:¹⁰ a high-T regime ($T > 405$ K, $E_A = 0.22$ eV) and a low-T regime ($T < 405$ K, $E_A = 0.7$ eV). For LYB, by contrast, the CHGNet_600K predictions for compressed cells align well with both AIMD results and experiments.

Analysis of mean-squared displacements (MSDs) and diffusivities reveals a clear contrast in Li-ion transport between LYC and LYB (Figure 4). In LYC, Li^+ diffusion is highly anisotropic, with diffusion coefficients at 500 K approximately 2 – 3 times larger along the c axis than within the ab -plane (Figures 4(a), (b)). Li^+ probability density maps (Figures 4(c)-(e)) reveal preferential migration through adjacent face-sharing octahedral sites along c over edge-sharing pathways in the ab -plane, with an intermediate tetrahedral site. This behavior is consistent with the layered structure providing open diffusion channels along c . In contrast,

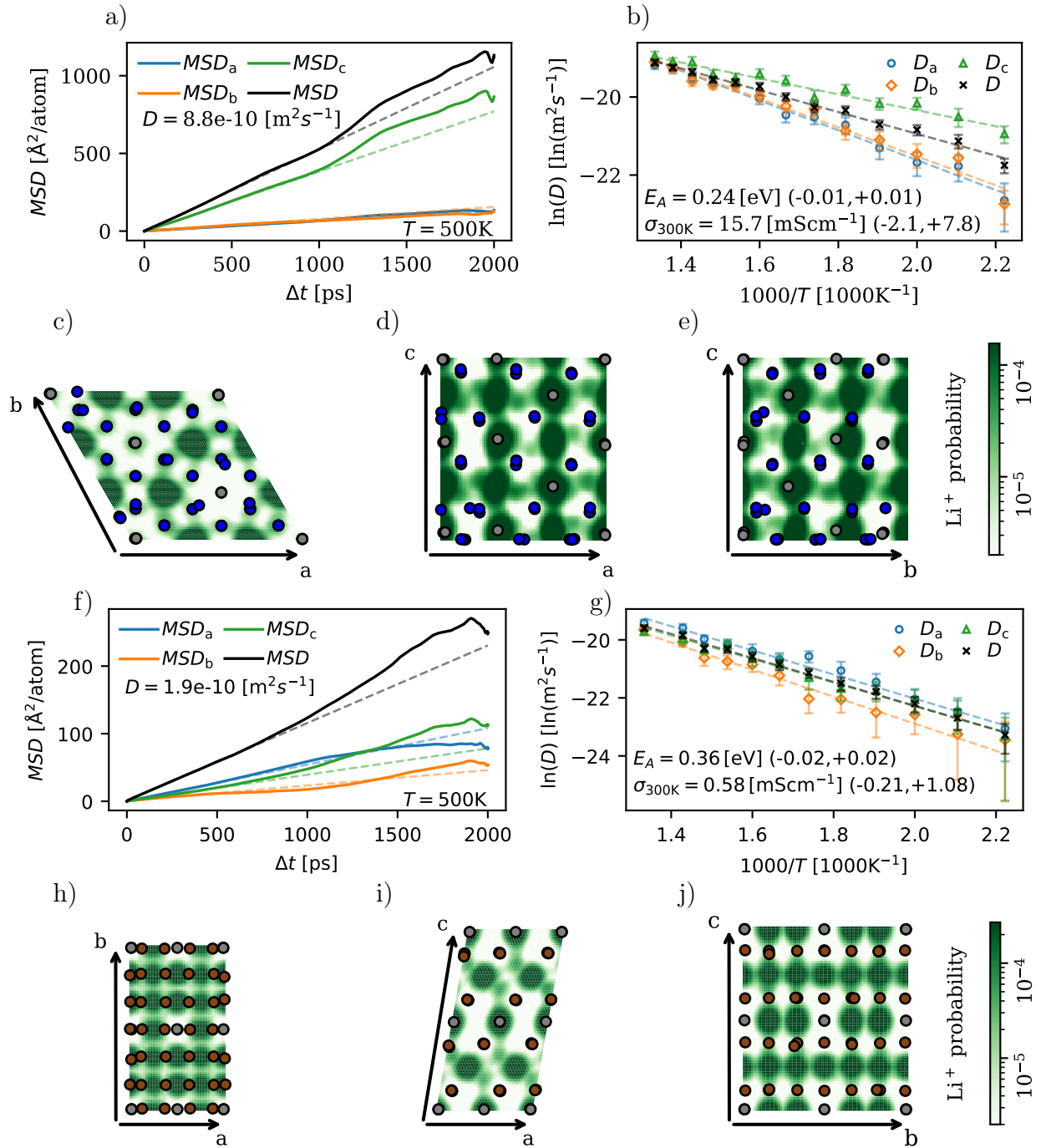


Figure 4: Li^+ transport properties of (a)-(e) LYC and (f)-(j) LYB, obtained from MD simulations in the NVT ensemble, starting from NpT -equilibrated structures ($p=10$ kbar), and using the CHGNet_600K potential. (a) and (f) MSD as a function of Δt at $T=500$ K; (b) and (g) temperature-dependence of the diffusion coefficient, in logarithmic scale; and (c)-(e) and (h)-(j) Li^+ probability density maps from MD simulations at $T=500$ K projected on the ab -, ac -, and bc -plane, respectively (Li: green, Y: gray, Cl: blue, Br: brown). Error bars are derived according to the procedure in Ref. 33.

LYB exhibits nearly isotropic diffusion with a diffusion coefficient of $1.9 \times 10^{-10} \text{ m}^2 \text{ s}^{-1}$ at 500 K. This isotropy reflects migration occurring exclusively via edge-sharing pathways with an intermediate tetrahedral site (Figures 4(f)-(j)).

Effect of halide substitution on phase stability and Li-ion transport

Last, we investigate the impact of Cl/Br substitution on phase stability and Li^+ transport across the mixed LYCB series. The phase stability is assessed from the total energy difference between the two competing phases – trigonal $P\bar{3}c1$ and monoclinic $C2$. Table 3 lists the calculated energy difference, $\Delta E = E_{P\bar{3}c1} - E_{C2}$, for $x = 0$ to 6, obtained from *ab initio* calculations (for details, see Figure S8). Comparable trends are reproduced using CHGNet_600K. The results reveal that the two phases are nearly degenerate, with energy differences of only a few meV/atom, suggesting the possibility of solid-solution behavior at finite temperatures due to thermal contributions. At Br-rich compositions ($x > 1.5$), the monoclinic $C2$ phase becomes thermodynamically favored, in agreement with the experimentally observed phase transition in the range $1.5 < x \leq 3$ reported in Ref. 9.

Table 3: Differences in total energy between the two phases, $\Delta E = E_{P\bar{3}c1} - E_{C2}$ for $x = 0$ to 6, expressed in meV/atom, obtained from DFT structure optimization. Negative ΔE indicate the $P\bar{3}c1$ phase is energetically favored, whereas positive ΔE mean that $C2$ is more stable. We note that these values may slightly vary depending on the ML model used in the structure enumeration and ranking procedure.

x_{Br}	ΔE (meV/atom)	x_{Br}	ΔE (meV/atom)
0.0	-2.27	3.5	4.30
0.5	-2.08	4.0	4.51
1.0	-0.82	4.5	4.41
1.5	-0.25	5.0	4.15
2.0	1.79	5.5	4.62
2.5	3.28	6.0	5.22
3.0	3.88		

Figure 5 presents Li^+ transport properties for various Br-rich LYCB compositions in the $C2$ crystal structure. As the Cl content increases (*i.e.*, $x = 6$ down to 3), the room-

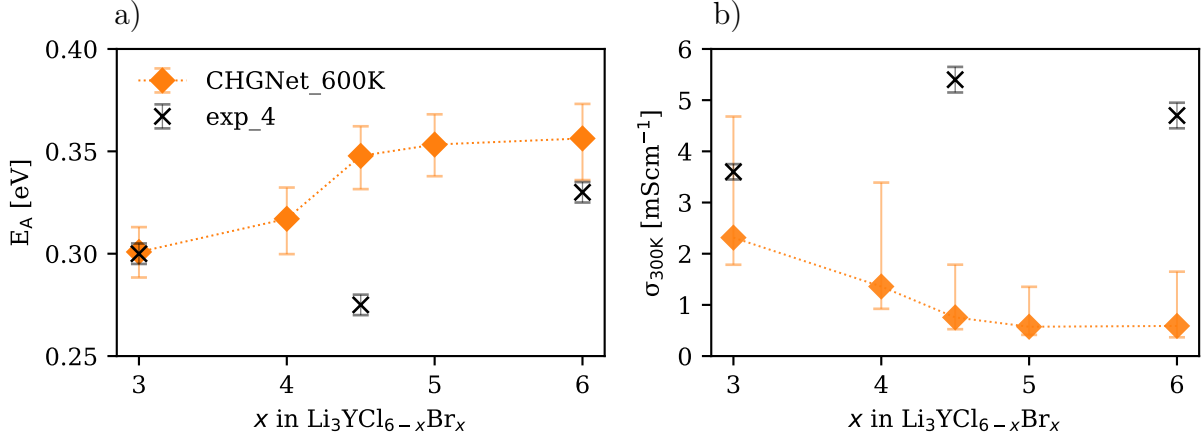


Figure 5: Li⁺ transport properties for LYCB obtained from CHGNet_600K MD simulations (starting from NpT -equilibrated structures under $p=10$ kbar), including (a) activation energy E_A and (b) room-temperature ionic conductivity σ_{300K} . We consider $C2$ -symmetry structures of LYCB with $x = 3$ to 6. Experimental values (exp_4⁹) are shown with black crosses.

temperature Li⁺ conductivity initially remains roughly constant around 0.7 mS.cm⁻¹, before increasing monotonically for $5.0 \geq x \geq 3.0$. This trend is inversely reflected in the activation energies and can be attributed to increased disorder and strain in the lattice, which lowers diffusion barriers. Although the experimentally reported conductivity maximum between $x = 3$ and $x = 6$ is not fully reproduced,⁹ the predicted values are close to experiment and indicate that σ_{300K} of LYB can be enhanced through Br \rightarrow Cl substitution. Analysis of MSDs, diffusion coefficients, and Li⁺ probability density maps for Li₃YCl₃Br₃ in Figure S9 shows isotropic transport behavior, qualitatively similar to the parent LYB system (with the same $C2$ parent space group).

Conclusions

In summary, this work establishes a data-efficient and transferable framework for modeling lithium transport in halide SEs via targeted fine-tuning of uMLIPs. Starting from experimentally refined disordered structures, we systematically enumerate and rank ordered configurations to identify physically meaningful low-energy models, which are then equilibrated under realistic thermodynamic conditions using MLIP-driven simulations. Fine-tuning the

CHGNet model on halide-specific data restores near-DFT accuracy in energy, force, and stress tensor predictions, stabilize NpT simulations up to 800 K, and enables nanosecond-scale MD simulations of Li^+ diffusion across the full LYCB composition range.

The fine-tuned CHGNet model achieves quantitative agreement with DFT and AIMD at a cost reduction exceeding four orders of magnitude, and remains transferable across the entire LYCB series. Beyond reproducing known behavior, it provides key insights into anisotropic Li^+ migration in LYC, isotropic transport in LYB, and the pressure- and composition-dependent modulation of ionic conductivity. More broadly, this work demonstrates that targeted fine-tuning of uMLIPs bridges the gap between efficiency and fidelity, providing a practical route for predictive modeling of complex, partially disordered materials that remain inaccessible to high-throughput DFT databases. Overall, the presented approach lays a groundwork for accelerating the discovery and optimization of next-generation SEs through integrated exploration of structure, properties, and transport.

Computational Methods

DFT calculations – DFT calculations are conducted with the Vienna Ab initio Simulation Package (VASP) ^{34,35} using the generalized gradient approximation (GGA) as proposed by Perdew–Burke–Ernzerhof (PBE).³⁶ The static calculations used to produce the training dataset are performed using a $3 \times 3 \times 3$ Γ -centered \mathbf{k} -point grid and a cutoff energy of 350 eV, ensuring energy is converged within 0.5 meV atom⁻¹. For structure optimization, we use a Γ -centered \mathbf{k} -point grid, with a \mathbf{k} -point-spacing of 0.2 \AA^{-1} , and a cutoff energy of 520 eV. Atomic positions and cell parameters are optimized with the FIRE³⁷ optimizer and a convergence threshold of 0.01 eV \AA^{-1} . The same optimizer and threshold are used for MLIP-based structure optimization. For the AIMD simulations, we use a timestep of 1 fs, a cutoff energy of 350 eV, a Nosé-Hoover thermostat in the NVT ensemble, and a $2 \times 2 \times 2$ Γ -centered \mathbf{k} -point grid. Finite-temperature volumes are predicted using an equation of state

approach, such that the initial cell volume is scaled by 0%, 5%, and 10%, and the resulting volumes are fitted to the corresponding NVT -equilibrated pressures (averaged over at least 1 ps after equilibration) using a quadratic function.

Structure enumeration and ranking – We start from the experimental LYC and LYB structures⁸ and build $1 \times 1 \times 2$ supercells containing 60 and 40 atoms, respectively. We enumerate all symmetrically distinct configurations using *enumlib*.²⁹ Total energy and formation energy are predicted with the *matgl* package,³⁸ using algorithms implemented in ASE³⁹ and different uMLIPs as calculators. M3GNet and CHGNet provide similar energy predictions, with the former being about 3 times faster – hence M3GNet is used for the ranking procedure here. Structure optimization is performed using the ASE optimizer, employing the FIRE algorithm and a convergence threshold of 0.01 eV \AA^{-1} . The results reported herein are generated using the following software versions: Python 3.10.10, Pymatgen 2025.2.18, PyTorch 2.4.0+cu124, ASE 3.23.0, M3GNet 0.2.4, CHGNet 0.3.8 (pretrained model CHGNet 0.3.0), sevnm 0.11.0 (pretrained model SEvEnNet-MF-ompa⁴⁰).

uMLIP fine-tuning procedure – The pretrained CHGNet uMLIP is fine-tuned to enable stable NpT MD simulations of LYCB structures at temperatures up to 800 K. The following iterative procedure is used (Figure 1):

- 1) Generate finite-temperature structures at T_i :
 - 1.1) Starting from the LYC0 and LYB0 structures, equilibrate the cell volume by NpT MD at T_i and 1 bar, using CHGNet_ T_{i-1}). Subsequently perform an NVT MD production run (1,000,000 steps; store configurations every 10th step).
 - 1.2) For each system, derive a subset of representative structures from the trajectory to ensure broad geometric diversity. Selection is performed using furthest-point sampling based on the mean-squared error in atomic positions.
- 2) Calculate energy, force, and stress labels using static DFT.
- 3) Fine-tune the CHGNet model with the labeled dataset, composed of 50% LYC and 50% LYB structures, yielding the fine-tuned CHGNet_ T_i model. The batch size, number of

epochs, initial learning rate, and number of frozen layers were optimized for this step, while all other hyperparameters were kept as in Ref. 15.

- 4) If $T_i < T_{max}$, the temperature is increased according to $T_{i+1} = T_i + \Delta T$, and the procedure is repeated from step 1.2).

This iterative strategy ensures that the structural configurations encountered during MD remain close to those represented in the progressively expanding training dataset, thereby maintaining stability and physical reliability of the simulations. The temperature increment ΔT controls the magnitude of structural perturbations between iterations and was set to 200 K. Step 1) required approximately 0.8 s/atom/picosecond on a GPU, while step 3) required $\sim 5-10$ minutes on a GPU for a dataset containing 150–300 structures per iteration. In each iteration, the model was fine-tuned incrementally using only the dataset generated at the current temperature, starting from the model obtained in the previous step.

uMLIP-driven MD simulations – MD simulations are performed with the GPU-accelerated LAMMPS package,^{41–47} using either the (finetuned) CHGNet^{15,48} or SevenNet-MF-ompa¹³ uMLIP. A timestep of 1 fs is used. Temperature coupling for NVT and NpT simulations is set to 0.1 ps and pressure coupling (for NpT) to 1 ps using the Nosé-Hoover thermostat and barostat.^{49,50} Prior to each NVT production run, the following equilibration procedure is carried out: velocities are initialized at 100 K and the system is linearly heated to the target temperature over 2 ps while keeping the cell parameters fixed. The system is then equilibrated for 50 ps in the NVT ensemble. For the NpT -equilibrated cells, this step is followed by an additional 140 ps equilibration at a target pressure of 1 bar. The final cell is defined by the average lattice parameters and volume over the last 112 ps of the NpT equilibration. For the 60- and 40-atoms LYC and LYB supercells, the computational cost on a GPU is approximately 0.8 s/atom/picosecond, *i.e.*, more than 10^5 times faster than a comparable AIMD simulation performed on a CPU.

Ionic conductivity derivation – From an MD trajectory of duration t at temperature T , ion transport properties including the self-diffusion coefficient, D , ionic conductivity, σ ,

and activation energy for diffusion, E_A , are obtained. First, the average atomic MSD over a time interval Δt for N atoms i is computed as:⁵¹

$$\text{MSD}(\Delta t) = \langle |\mathbf{r}(\Delta t)|^2 \rangle = \frac{1}{N} \sum_i \langle |\mathbf{r}_i(t_0 + \Delta t) - \mathbf{r}_i(t_0)|^2 \rangle_{t_0} \quad (1)$$

where Δt is a time interval with an upper bound given by the total simulation time t , t_0 is a given timestep with $t_0 \in [0, t - \Delta t]$, and $\langle \rangle_{t_0}$ indicates an average over all possible t_0 . The lithium self-diffusion coefficient D at temperature T is obtained from the Einstein relation:⁵²

$$D = \lim_{\Delta t \rightarrow \infty} \frac{\text{MSD}(\Delta t)}{2d\Delta t} \quad (2)$$

where d is the dimensionality of diffusion (*e.g.*, $d = 3$ for 3D diffusion). In practice, D is determined from a linear fit to discrete $\text{MSD}(\Delta t)$ data. To ensure a reliable fit, the ballistic diffusion regime at short times ($0 < \Delta t < x \text{ ps}$) and the region with poor statistics at large lag times ($\Delta t > 0.7t$) are excluded, following Ref 33. As the calculated $\text{MSD}(\Delta t)$ exhibits deviations from linear behavior beyond approximately 500 – 1000 ps, the maximum fitting window was limited to $\Delta t_{max} = 500 \text{ ps}$. Error bars in D are estimated according to the procedure described in Ref. 33. Activation energies for diffusion are obtained by fitting $\ln(D)$ versus $1/T$ over multiple temperature using the Arrhenius relation:

$$D(T) = \tilde{D} \exp\left(-\frac{E_A}{k_B T}\right) \quad (3)$$

where \tilde{D} is the constant diffusion coefficient for $T \rightarrow \infty$. If N mobile ions of charge q are present in a system of volume V , the ionic conductivity σ is calculated via the Nernst-Einstein relation:^{52,53}

$$\sigma(T) = \frac{Nq^2}{Vk_B T} \cdot D(T). \quad (4)$$

Supporting Information Available

The Supplementary Information is available free of charge.

- Fine-tuning dataset at finite-temperature; Transferability across various test sets; Alternative accumulative fine-tuning approach; Optimization of cell parameters; Formation energies and phase stability prediction; Lithium-ion diffusion in $\text{Li}_3\text{YCl}_3\text{Br}_3$ (PDF).
- Training dataset; all fine-tuned CHGNet models; low-energy LYCB structures from ranking (zip).

Acknowledgement

The authors thank Francesco Ricci, Yusuf Shaidu, and Dany Carlier for stimulating discussions, Zhenming Xu for providing additional information on Ref 54, Bassem Sboui for computational support, and Miguel Ceja for support with the Vesta package. The calculations were primarily supported by the computing facilities provided by the Mésocentre de Calcul Intensif Aquitain (MCIA) of the University of Bordeaux. The authors thank the French National Research Agency (STORE-EX Labex Project ANR-10-LABX-76-01) for financial support.

References

- (1) Daniel, C. Materials and processing for lithium-ion batteries. *JOM* **2008**, *60*, 43–48.
- (2) Goodenough, J. B.; Park, K.-S. The Li-Ion Rechargeable Battery: A Perspective. *Journal of the American Chemical Society* **2013**, *135*, 1167–1176.
- (3) Ohno, S.; Banik, A.; Dewald, G. F.; Kraft, M. A.; Krauskopf, T.; Minafra, N.; Till, P.; Weiss, M.; Zeier, W. G. Materials design of ionic conductors for solid state batteries. *Progress in Energy* **2020**, *2*, 022001.

- (4) Janek, J.; Zeier, W. G. Challenges in speeding up solid-state battery development. *Nature Energy* **2023**, *8*, 230–240.
- (5) Kerman, K.; Luntz, A.; Viswanathan, V.; Chiang, Y.-M.; Chen, Z. Review—Practical challenges hindering the development of solid-state Li-ion batteries. *Journal of The Electrochemical Society* **2017**, *164*, A1731–A1744.
- (6) Pasta, M.; others Energy 2020 roadmap on solid-state batteries. *Journal of Physics: Energy* **2020**, *2*, 032008.
- (7) Asano, T.; Sakai, A.; Ouchi, S.; Sakaida, M.; Miyazaki, A.; Hasegawa, S. Solid Halide Electrolytes with High Lithium-Ion Conductivity for Application in 4 V Class Bulk-Type All-Solid-State Batteries. *Advanced Materials* **2018**, *30*, 1803075.
- (8) Schlem, R.; Banik, A.; Ohno, S.; Suard, E.; Zeier, W. G. Insights into the Lithium Sub-structure of Superionic Conductors Li₃YCl₆ and Li₃YBr₆. *Chemistry of Materials* **2021**, *33*, 327–337, Publisher: American Chemical Society.
- (9) van der Maas, E.; Zhao, W.; Cheng, Z.; Famprakis, T.; Thijs, M.; Parnell, S. R.; Ganapathy, S.; Wagemaker, M. Investigation of Structure, Ionic Conductivity, and Electrochemical Stability of Halogen Substitution in Solid-State Ion Conductor Li₃YBr_xCl_{6-x}. *The Journal of Physical Chemistry C* **2023**, *127*, 125–132, Publisher: American Chemical Society.
- (10) Liu, Z.; Chien, P.-H.; Wang, S.; Song, S.; Lu, M.; Chen, S.; Xia, S.; Liu, J.; Mo, Y.; Chen, H. Tuning collective anion motion enables superionic conductivity in solid-state halide electrolytes. *Nature Chemistry* **2024**, *16*, 1584–1591.
- (11) Wang, G.; Wang, C.; Zhang, X.; Li, Z.; Zhou, J.; Sun, Z. Machine learning interatomic potential: Bridge the gap between small-scale models and realistic device-scale simulations. *iScience* **2024**, *27*, 109673.

- (12) Jacobs, R. et al. A practical guide to machine learning interatomic potentials – Status and future. *Current Opinion in Solid State and Materials Science* **2025**, *35*, 101214.
- (13) Park, Y.; Kim, J.; Hwang, S.; Han, S. Scalable Parallel Algorithm for Graph Neural Network Interatomic Potentials in Molecular Dynamics Simulations. *J. Chem. Theory Comput.* **2024**, *20*, 4857–4868.
- (14) Chen, C.; Ong, S. P. A universal graph deep learning interatomic potential for the periodic table. *Nature Computational Science* **2022**, *2*, 718–728.
- (15) Deng, B.; Zhong, P.; Jun, K.; Riebesell, J.; Han, K.; Bartel, C. J.; Ceder, G. CHGNet as a pretrained universal neural network potential for charge-informed atomistic modelling. *Nature Machine Intelligence* **2023**, *5*, 1031–1041.
- (16) Jain, A.; Ong, S. P.; Hautier, G.; Chen, W.; Richards, W. D.; Dacek, S.; Cholia, S.; Gunter, D.; Skinner, D.; Ceder, G.; Persson, K. A. Commentary: The Materials Project: A materials genome approach to accelerating materials innovation. *APL Materials* **2013**, *1*, 011002.
- (17) Deng, B. Materials Project Trajectory (MPtrj) Dataset. 2023; https://figshare.com/articles/dataset/Materials_Project_Trajectory_MPtrj_Dataset/23713842/2, Artwork Size: 12188168685 Bytes Pages: 12188168685 Bytes.
- (18) Barroso-Luque, L.; Shuaibi, M.; Fu, X.; Wood, B. M.; Dzamba, M.; Gao, M.; Rizvi, A.; Zitnick, C. L.; Ulissi, Z. W. Open Materials 2024 (OMat24) Inorganic Materials Dataset and Models. 2024; <https://arxiv.org/abs/2410.12771>.
- (19) Liu, X.; Zeng, K.; Wang, Y.; Zhao, T. A Study on the Fine-Tuning Performance of Universal Machine-Learned Interatomic Potentials (U-MLIPs). 2025; <https://arxiv.org/abs/2506.07401>, Version Number: 1.

- (20) Huang, X.; Deng, B.; Zhong, P.; Kaplan, A. D.; Persson, K. A.; Ceder, G. Cross-functional transferability in universal machine learning interatomic potentials. 2025; <https://arxiv.org/abs/2504.05565>, Version Number: 1.
- (21) Kaur, H.; Della Pia, F.; Batatia, I.; Advincula, X. R.; Shi, B. X.; Lan, J.; Csányi, G.; Michaelides, A.; Kapil, V. Data-efficient fine-tuning of foundational models for first-principles quality sublimation enthalpies. *Faraday Discussions* **2025**, *256*, 120–138.
- (22) Radova, M.; Stark, W. G.; Allen, C. S.; Maurer, R. J.; Bartók, A. P. Fine-tuning foundation models of materials interatomic potentials with frozen transfer learning. *npj Computational Materials* **2025**, *11*, 237.
- (23) Li, Z.; Kermode, J. R.; De Vita, A. Molecular Dynamics with On-the-Fly Machine Learning of Quantum-Mechanical Forces. *Phys. Rev. Lett.* **2015**, *114*, 096405.
- (24) Shapeev, A. V. Moment Tensor Potentials: A Class of Systematically Improvable Interatomic Potentials. *Multiscale Modeling & Simulation* **2016**, *14*, 1153–1173.
- (25) Bernstein, N.; Csányi, G.; Deringer, V. L. De novo exploration and self-guided learning of potential-energy surfaces. *npj Computational Materials* **2019**, *5*, 99.
- (26) Vandermause, J.; Torrisi, S. B.; Batzner, S.; Xie, Y.; Sun, L.; Kolpak, A. M.; Kozinsky, B. On-the-fly active learning of interpretable Bayesian force fields for atomistic rare events. *npj Computational Materials* **2020**, *6*, 20.
- (27) Ewald, P. P. Die Berechnung optischer und elektrostatischer Gitterpotentiale. *Annalen der Physik* **1921**, *369*, 253–287.
- (28) Toukmaji, A. Y.; Board, J. A. Ewald summation techniques in perspective: a survey. *Computer Physics Communications* **1996**, *95*, 73–92.
- (29) Hart, G. L. W.; Forcade, R. W. Algorithm for generating derivative structures. *Physical Review B* **2008**, *77*, 224115.

- (30) Park, Y.; Kim, J.; Kim, J.; Jeon, H.; Han, S. SevenNet_MF_ompa. 2025; https://figshare.com/articles/software/7net_MF_ompa/28590722/7, Artwork Size: 412242578 Bytes Pages: 412242578 Bytes.
- (31) Wang, S.; Bai, Q.; Nolan, A. M.; Liu, Y.; Gong, S.; Sun, Q.; Mo, Y. Lithium Chlorides and Bromides as Promising Solid-State Chemistries for Fast Ion Conductors with Good Electrochemical Stability. *Angewandte Chemie International Edition* **2019**, *58*, 8039–8043.
- (32) Lejaeghere, K. et al. Reproducibility in density functional theory calculations of solids. *Science* **2016**, *351*, aad3000.
- (33) He, X.; Zhu, Y.; Epstein, A.; Mo, Y. Statistical variances of diffusional properties from ab initio molecular dynamics simulations. *npj Computational Materials* **2018**, *4*, 18.
- (34) Kresse, G.; Furthmüller, J. Efficient iterative schemes for *ab initio* total-energy calculations using a plane-wave basis set. *Physical Review B* **1996**, *54*, 11169–11186.
- (35) Kresse, G.; Joubert, D. From ultrasoft pseudopotentials to the projector augmented-wave method. *Physical Review B* **1999**, *59*, 1758–1775.
- (36) Perdew, J. P.; Burke, K.; Ernzerhof, M. Generalized Gradient Approximation Made Simple. *Physical Review Letters* **1996**, *77*, 3865–3868.
- (37) Bitzek, E.; Koskinen, P.; Gähler, F.; Moseler, M.; Gumbusch, P. Structural relaxation made simple. *Physical Review Letters* **2006**, *97*, 170201.
- (38) Ko, T. W.; Deng, B.; Nassar, M.; Barroso-Luque, L.; Liu, R.; Qi, J.; Liu, E.; Ceder, G.; Miret, S.; Ong, S. P. Materials Graph Library (MatGL), an open-source graph deep learning library for materials science and chemistry. 2025; <https://arxiv.org/abs/2503.03837>, Version Number: 1.

- (39) Hjorth Larsen, A. et al. The atomic simulation environment—a Python library for working with atoms. *Journal of Physics: Condensed Matter* **2017**, *29*, 273002.
- (40) Kim, J.; Kim, J.; Kim, J.; Lee, J.; Park, Y.; Kang, Y.; Han, S. Data-Efficient Multifidelity Training for High-Fidelity Machine Learning Interatomic Potentials. *J. Am. Chem. Soc.* **2024**, *147*, 1042–1054.
- (41) Thompson, A. P.; Aktulga, H. M.; Berger, R.; Bolintineanu, D. S.; Brown, W. M.; Crozier, P. S.; In 'T Veld, P. J.; Kohlmeyer, A.; Moore, S. G.; Nguyen, T. D.; Shan, R.; Stevens, M. J.; Tranchida, J.; Trott, C.; Plimpton, S. J. LAMMPS - a flexible simulation tool for particle-based materials modeling at the atomic, meso, and continuum scales. *Computer Physics Communications* **2022**, *271*, 108171.
- (42) Brown, W. M.; Wang, P.; Plimpton, S. J.; Tharrington, A. N. Implementing molecular dynamics on hybrid high performance computers – short range forces. *Computer Physics Communications* **2011**, *182*, 898–911.
- (43) Brown, W. M.; Kohlmeyer, A.; Plimpton, S. J.; Tharrington, A. N. Implementing molecular dynamics on hybrid high performance computers – Particle–particle particle–mesh. *Computer Physics Communications* **2012**, *183*, 449–459.
- (44) Brown, W. M.; Yamada, M. Implementing molecular dynamics on hybrid high performance computers—Three-body potentials. *Computer Physics Communications* **2013**, *184*, 2785–2793.
- (45) Nguyen, T. D.; Plimpton, S. J. Accelerating dissipative particle dynamics simulations for soft matter systems. *Computational Materials Science* **2015**, *100*, 173–180.
- (46) Nguyen, T. D. GPU-accelerated Tersoff potentials for massively parallel Molecular Dynamics simulations. *Computer Physics Communications* **2017**, *212*, 113–122.

- (47) Nikolskiy Vsevolod; Stegailov Vladimir *Advances in Parallel Computing*; IOS Press, 2020.
- (48) Corporation, A. Customized LAMMPS (2Aug2023) for Neural Network Potential. <https://github.com/advancesoftcorp/lammps>, 2023; Accessed: 2025-05-16.
- (49) Nosé, S. A molecular dynamics method for simulations in the canonical ensemble. *Molecular Physics* **1984**, *52*, 255–268.
- (50) Hoover, W. G. Canonical dynamics: Equilibrium phase-space distributions. *Physical Review A* **1985**, *31*, 1695–1697.
- (51) Ong, S. P.; Mo, Y.; Richards, W. D.; Miara, L.; Lee, H. S.; Ceder, G. Phase stability, electrochemical stability and ionic conductivity of the $\text{Li}_{10\pm 1}\text{MP}_2\text{X}_{12}$ ($\text{M} = \text{Ge}, \text{Si}, \text{Sn}, \text{Al}$ or P , and $\text{X} = \text{O}, \text{S}$ or Se) family of superionic conductors. *Energy Environ. Sci.* **2013**, *6*, 148–156, Publisher: Royal Society of Chemistry (RSC).
- (52) Baktash, A.; Reid, J. C.; Roman, T.; Searles, D. J. Diffusion of lithium ions in Lithium-argyrodite solid-state electrolytes. *npj Computational Materials* **2020**, *6*, Publisher: Springer Science and Business Media LLC.
- (53) Evans, D. J.; Morriss, G. P. *Statistical Mechanics of Nonequilibrium Liquids*, 1st ed.; ANU Press, 2007.
- (54) Xu, Z.; Duan, H.; Dou, Z.; Zheng, M.; Lin, Y.; Xia, Y.; Zhao, H.; Xia, Y. Machine learning molecular dynamics simulation identifying weakly negative effect of polyanion rotation on Li-ion migration. *npj Computational Materials* **2023**, *9*, Publisher: Springer Science and Business Media LLC.